

24 results.

25

26 *Keywords:* Large-eddy simulation; Chemical percolation devolatilization; Pulverized-coal
27 combustion; Partially stirred reactor

28

29 **1. Introduction**

30 Coal has been used to supply approximately 40% of worldwide electric power consumption [1],
31 and pulverized-coal combustion (PCC) is widely utilized in most of coal-fired power plants [2]. In
32 the foreseeable future, it can be expected that the utilization of coal will continue due to its good
33 availability [3]. Especially in China, where more than 70% of the electricity is generated from coal
34 combustion, the role of coal in the energy supply will continuously be significant in the near and
35 medium future [4]. On the other hand, burning a large amount of coal also leads to serious
36 environmental issues, such as haze in China. Recently more than 99% of the 500 largest cities in
37 China fail to meet the air quality standards prescribed by the world health organization (WHO) [5].
38 Therefore, development of clean coal technologies is crucially important and urgent [6,7].

39 To advance clean coal technologies, a comprehensive understanding of pulverized-coal
40 combustion physics is necessary. Numerical analysis is now an important research tool in this area,
41 together with advanced measurement techniques. As the sustained sharp increase of computing
42 capacity continues, large-eddy simulation (LES) has been used for pulverized-coal combustion (PCC)
43 research since its first use [8]. PCC-LES for large-scale coal-fired furnaces showed that LES could
44 achieve proper predictions of unsteady turbulence-combustion interactions [9-12]. Recently,
45 PCC-LES studies have mainly focused on laboratory-scale pulverized-coal jet flames. Yamamoto et

46 al. [13] and Pedel et al. [14] applied LES to a pulverized-coal jet flame ignited by a preheated gas
47 flow [15] and compared the predicted flame lift-off height, gas temperature and coal burnout with
48 experimental data. Another laboratory-scale pulverized-coal jet flame stabilized with a methane pilot
49 measured [16] at the Japanese Central Research Institute of Electric Power Industry (CRIEPI) has
50 also been used as a reference case, e.g. by Franchetti et al. [17] and Stein et al. [4], for validation
51 purposes. The velocity field statistics of the simulations agreed well with the measurements, but the
52 notable deviation of the scalar statistics reflected the complexity of PCC modeling. This
53 pulverized-coal jet flame will also be investigated in the present study. More recently, Rabaçal et al.
54 [18] carried out large-scale LES of pulverized-coal combustion in a laboratory-scale furnace and
55 good agreement with experimental measurements was achieved. Hara et al. [19] developed a global
56 volatile matter reaction scheme based on a detailed reaction mechanism and validated it by a direct
57 numerical simulation (DNS) of the CRIEPI coal jet flame. On the other hand, tabulated chemistry,
58 e.g., the flamelet approach, has been applied in PCC-LES recently by Watanabe et al. [20] and
59 Knappstein et al. [3].

60 The difficulty of achieving proper predictions of pulverized-coal combustion stems from
61 complex multi-physics coal combustion phenomena, which includes three main stages: pyrolysis,
62 volatile combustion and char combustion. The modeling accuracy of pyrolysis has been shown to
63 have a significant impact on coal combustion prediction [21,22]. Most numerical simulations of PCC
64 use a simplified pyrolysis model, i.e., the single first-order reaction model (SFOM) proposed by
65 Badzioch & Hawskley [23], to save computational cost [4]. However, the kinetic parameters in this
66 model can vary remarkably with the coal type and the heating rate. Directly using the reaction
67 parameters in technical literature can lead to unacceptable errors [24]. Hence, in recent PCC studies

68 [4,17,18,25] the SFOM pyrolysis model was a-priori calibrated by the chemical percolation
69 devolatilization (CPD) model [26], which is one of the detailed pyrolysis models. However,
70 incorporating the CPD model directly into the LES framework would further improve the accuracy
71 of PCC-LES. In our previous study on LES of pulverized-coal pyrolysis with no combustion
72 included, the performance of the CPD-incorporated LES (CPD-LES) method was confirmed [27].
73 For the second stage of coal combustion, the volatile combustion is popularly modeled with the eddy
74 break-up model (EBU) or eddy dissipation model (EDM) [28]. However, these models assumed
75 infinitely fast chemistry, which means the reaction rate is fully determined by turbulent mixing time
76 scales and chemical time scales are not accounted [3]. Finally, the char combustion, i.e., the third
77 stage of coal combustion, is often modeled using the kinetic/diffusion surface reaction model
78 proposed by Baum & Street [29], with both the intrinsic chemical reaction on the internal surface of
79 a char particle and the diffusion of gaseous oxidant through the film layer around the particle
80 considered.

81 In the present study, the developed CPD-incorporated LES methodology has been used to
82 investigate a pulverized-coal combustion case, and its performance is evaluated. The aim of this
83 study is to investigate PCC-LES using advanced pyrolysis and volatile combustion models. The CPD
84 model, which has been directly incorporated into the LES framework, provides the pyrolysis kinetics
85 for each pulverized-coal particle according to its local, instantaneous heating rate [27]. Volatile
86 combustion is modeled using the partially stirred reactor (PaSR) model adapted for LES [30], which
87 takes into consideration both subgrid turbulent mixing and chemical time scales time scales with
88 finite-rate chemistry. Char combustion is modeled by the kinetic/diffusion surface reaction model [29]
89 incorporates both the intrinsic chemical reaction on the internal surface of a char particle and the

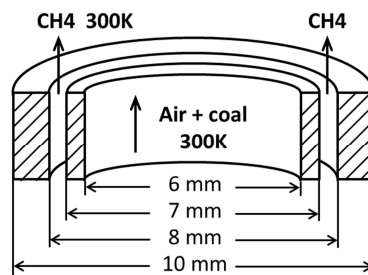
90 diffusion of gaseous oxidant through the film layer around the particle. The pulverized-coal jet flame
91 measured at the CRIEPI is simulated. The LES results will be compared with both experimental data
92 [16] and also previous PCC-LES results [17].

93

94 2. Pulverized-coal jet flame

95 A laboratory-scale methane-piloted pulverized-coal jet flame (Fig. 1) was measured at the
96 CRIEPI [16]. Coal particles are carried by airflow through the central nozzle, the inner diameter of
97 which is 6 mm. To stabilize the pulverized-coal jet flame, a methane annular pilot jet flame is used to
98 ignite coal particles. The Newland bituminous coal [16] was used in the experiments and its
99 properties are listed in Table 1. Because of the abundant experimental data available, this
100 pulverized-coal jet flame has been used as a reference case in RANS- [21,22,31], LES- [4,17] and
101 DNS-based [19] numerical studies for validation purposes.

102



103

104 Fig. 1. The inlet nozzle of the CRIEPI burner. Methane flow rate: $2.33 \times 10^{-5} \text{ m}^3/\text{s}$; pulverized-coal
105 feeding rate: $1.49 \times 10^{-4} \text{ kg/s}$; air flow rate: $2.07 \times 10^{-4} \text{ m}^3/\text{s}$. The air flow rate has been adjusted by
106 taking into consideration the air aspirated from the pulverized-coal feeder [22], and the Reynolds
107 number is ~ 2900 .

108

109

Table 1. Coal properties [16].

<i>Proximate analysis (wt%)</i>	
Moisture ^a	2.60
Ash ^b	15.20
Volatile matter ^b	26.90
Fixed carbon ^b	57.90
<i>Ultimate analysis (wt%)</i>	
Carbon ^b	71.90
Hydrogen ^b	4.40
Nitrogen ^b	1.50
Oxygen ^b	6.53
Sulfur ^b	0.44
Higher heating value ^b	29.1 MJ/kg
Lower heating value ^b	28.1 MJ/kg

111 ^a As received.

112 ^b Dry basis.

113

114 **3. Methodology**

115 *3.1. Gas phase modeling*

116 The governing equations for the gas and coal-particle phases are solved in the Eulerian and
 117 Lagrangian frameworks, respectively [27,32-35]. The filtered three-dimensional Navier-Stokes (NS)
 118 equations in the low-Mach-number form for mass, momentum, species and temperature are solved

119 for the gas phase:

$$120 \quad \frac{\partial \bar{\rho}}{\partial t} + \frac{\partial \bar{\rho} \tilde{u}_j}{\partial x_j} = \bar{S}_{m,p} \quad , \quad (1)$$

$$121 \quad \frac{\partial \bar{\rho} \tilde{u}_i}{\partial t} + \frac{\partial \bar{\rho} \tilde{u}_i \tilde{u}_j}{\partial x_j} = -\frac{\partial \bar{p}}{\partial x_i} + \frac{\partial}{\partial x_j} (\bar{\tau}_{ij} - q_{sgs,mom,ij}) + \bar{S}_{mom,p,i} \quad , \quad (2)$$

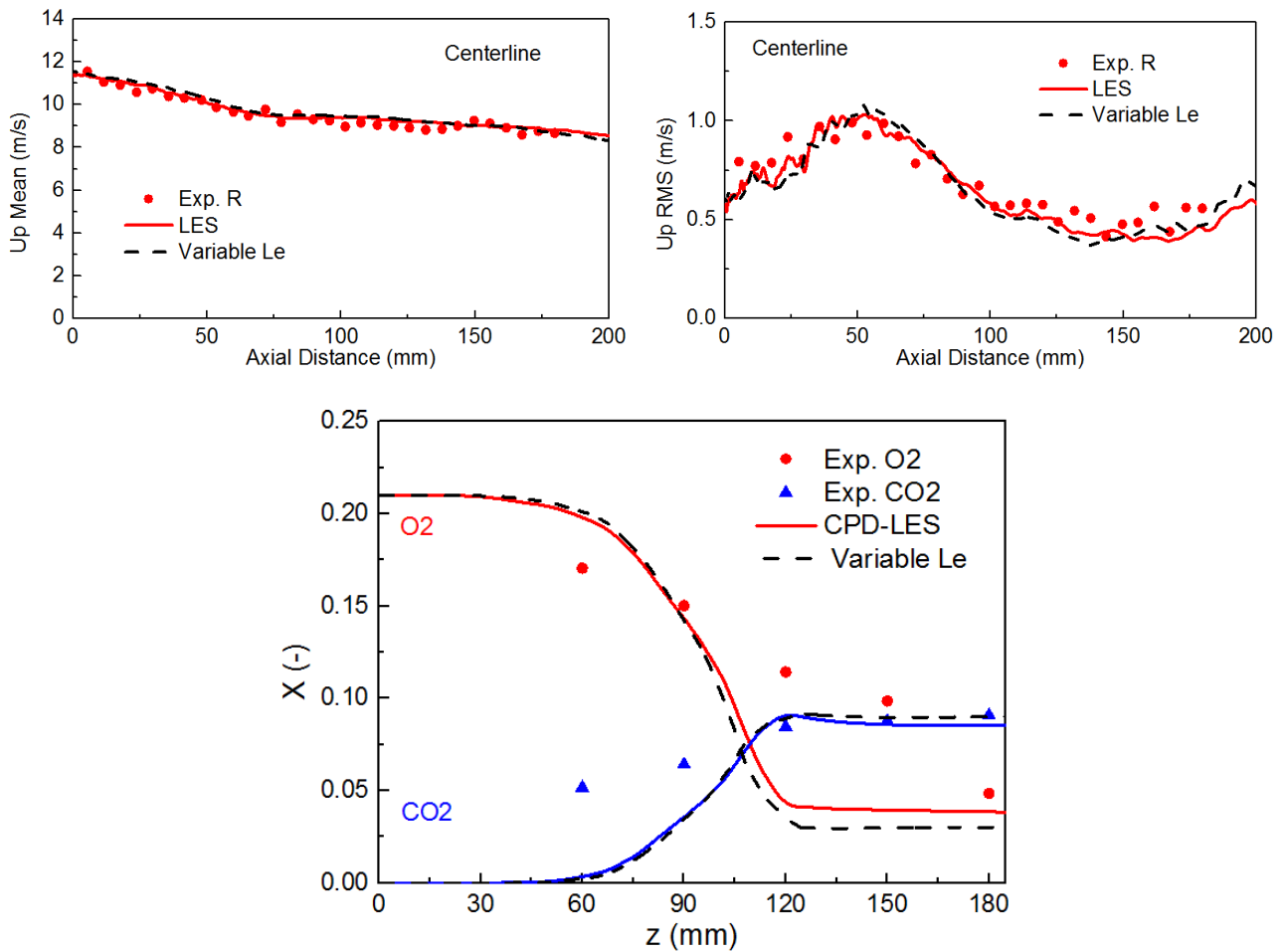
$$122 \quad \frac{\partial \bar{\rho} \tilde{Y}_n}{\partial t} + \frac{\partial \bar{\rho} \tilde{u}_j \tilde{Y}_n}{\partial x_j} = \frac{\partial}{\partial x_j} \left(\bar{\rho} \bar{D}_{diff} \frac{\partial \tilde{Y}_n}{\partial x_j} - q_{sgs,Y,n,j} \right) + \bar{\omega}_{Y,n} + \bar{S}_{Y,p,n} \quad , \quad (3)$$

$$123 \quad \frac{\partial \bar{\rho} \tilde{T}}{\partial t} + \frac{\partial \bar{\rho} \tilde{u}_j \tilde{T}}{\partial x_j} = \frac{\partial}{\partial x_j} \left(\frac{\bar{\lambda}}{\bar{C}_{P,g}} \frac{\partial \tilde{T}}{\partial x_j} - q_{sgs,T,j} \right) + \frac{\bar{\lambda}}{\bar{C}_{P,g}^2} \frac{\partial \bar{C}_{P,g}}{\partial x_j} \frac{\partial \tilde{T}}{\partial x_j} + \bar{\omega}_T + \bar{S}_{T,p} + \bar{S}_{T,R} \quad , \quad (4)$$

124 where $\bar{\rho}$ is the density of the gas mixture (kg/m³), \tilde{u}_j is gas velocity (m/s), \tilde{Y}_n is the mass
 125 fraction of the n th chemical species, \tilde{T} is gas temperature (K). The pressure is denoted by \bar{p} , and
 126 $\bar{\tau}_{ij} = \bar{\mu} (\partial \tilde{u}_i / \partial x_j + \partial \tilde{u}_j / \partial x_i) - \frac{2}{3} \bar{\mu} (\partial \tilde{u}_k / \partial x_k) \delta_{ij}$ is the viscous stress tensor. \bar{D}_{diff} is the molecular
 127 mass diffusivity coefficient (m²/s), $\bar{\lambda}$ and $\bar{C}_{P,g}$ are the thermal conductivity (W/m K) and specific
 128 heat capacity (J/kg K) of the gas mixture. The subgrid-scale (SGS) terms, $q_{sgs,mom,ij}$, $q_{sgs,Y,n,j}$ and $q_{sgs,T,j}$,
 129 are calculated by the Germano dynamic model [36]. The transport equations for the species of N₂, O₂,
 130 H₂O, CO₂, CH₄, CO, C₂H₂, H₂ and tar are solved. Pulverized-coal particles are modeled as point
 131 sources and two-way interactions between the gas phase and particles are considered. $\bar{S}_{m,p}$,
 132 $\bar{S}_{mom,p,i}$, $\bar{S}_{Y,p,n}$ and $\bar{S}_{T,p}$ are the two-way coupling terms due to the effects of particles on the gas
 133 phase. The drag effects are also included. $\bar{\omega}_{Y,n}$ is the chemical reaction source term due to gas
 134 phase combustion. In the temperature equation, the radiative heat transfer ($\bar{S}_{T,R}$), heat exchange
 135 between the gas phase and coal particles ($\bar{S}_{T,p}$), and heat release of gas phase combustion ($\bar{\omega}_T$) are
 136 considered. In the present study, the Lewis number (Le = 1.0) and Prandtl number (Pr = 0.7) are
 137 assumed to be constant. The impact of the unity Lewis number assumption has been investigated by
 138 comparing LES results between two cases with unity and variable Lewis numbers, respectively, and

139 is found to be minor (see Fig. 2). The molecular viscosity ($\bar{\mu}$) is determined using the Sutherland's
 140 Law [37] of N_2 , considering N_2 is the major species of the gas mixture. The molecular mass
 141 diffusivity and thermal conductivity are calculated based on the constant Lewis and Prandtl numbers.

142



143

144

145 Fig. 2. Comparison of LES results on the mean and RMS streamwise velocities of coal particles and
 146 the mole fractions of O_2 and CO_2 along the jet centerline between two cases with unity and variable
 147 Lewis numbers.

148

149 3.2. Particle phase modeling

150 The momentum equation of a Lagrangian coal particle can be written as:

151

$$\frac{du_{p,j}}{dt} = \frac{f}{\tau_p} (\tilde{u}_j - u_{p,j}) + W_{sgs,j} \quad (5)$$

152

where $u_{p,j}$ is the velocity of the particle (m/s). The dynamic response time of a particle (s) is

153

$\tau_p = \rho_p d_p^2 / 18\bar{\mu}$, ρ_p particle density (kg/m³), d_p particle diameter (m). f is the drag coefficient.

154

Following Jones et al. [38], a stochastic Markov model is used to incorporate the effects of

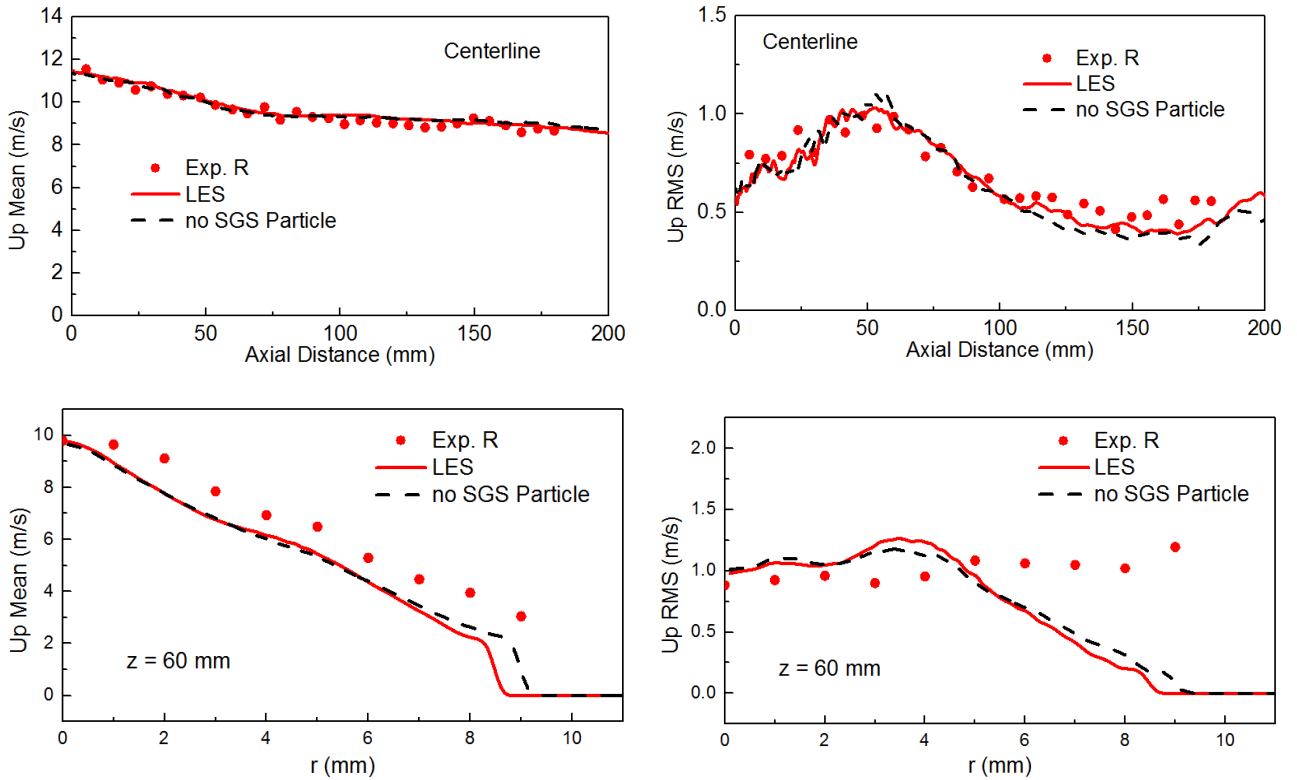
155

unresolved SGS turbulence ($W_{sgs,j}$) into particle acceleration, although only minor differences were

156

found between the results of the LESs including or excluding this model (see Fig. 3).

157



158

159

160

Fig. 3. Comparison of LES results on the mean and RMS streamwise velocities of coal particles

161

along the jet centerline and at $z = 60$ mm between two cases with the stochastic Markov model

162

enabled and disabled.

163

164

The particle temperature is obtained by solving:

165
$$\frac{dT_p}{dt} = \frac{(Q_{conv} + Q_{rad} + Q_{dev} + Q_{char})}{m_p C_{p,p}}, \quad (6)$$

166 where T_p is the temperature of the particle (K), m_p mass (kg), $C_{p,p}$ specific heat capacity (J/kg K).

167 The heat transfer due to convection, radiation, pyrolysis (devolatilization) and char combustion are

168 $Q_{conv} = Nu C_{p,g} m_p (\tilde{T} - T_p) / 3 Pr \tau_p$, $Q_{rad} = \varepsilon_p \pi d_p^2 \sigma (T_R^4 - T_p^4)$, $Q_{dev} = -\Delta h_{dev} dm_{vol}/dt$, and

169 $Q_{char} = -\Delta h_{char} dm_{char}/dt$. Nu is the Nusselt number calculated by the Ranz-Marshall correlations

170 [39]. The radiation temperature (K) is estimated by $T_R = (G/4\sigma)^{1/4}$, where G is the incident

171 radiation (W/m^2) determined by the Discrete Ordinates Method (DOM) [17,18,40]. σ is the

172 Stefan-Boltzmann constant ($5.67 \times 10^{-8} W/m^2 K^4$). The particle emissivity ε_p is set to 0.9 [41]. The

173 gas absorption coefficient is determined by the weighted-sum-of-the-gray-gases model (WSGGM)

174 [42].

175 In the solver, the radiative transfer equation is solved using DOM on its own and not coupled

176 with the temperature fields, which are predicted by the energy equations of the two phases. The

177 solving procedure is as follows: the temperature obtained in the previous time step is used for

178 iteratively solving the radiative transfer equation for radiation intensity I . The incident radiation G

179 can then be obtained via $G = \int_0^{4\pi} I d\Omega$ to calculate the radiation source terms in the two energy

180 equations. The gas and particle temperatures in the current time step are then updated finally.

181 Finally, the rate of change of the mass of each coal particle (dm_p/dt) is equal to the sum of the

182 coal pyrolysis rate (dm_{vol}/dt) and char combustion rate (dm_{char}/dt), which will be discussed in Section

183 3.3. Since the moisture content of the coal in the present study is relatively low (see Table 1), drying

184 is not considered, as in Stein et al. [4].

185

186 3.3. Coal pyrolysis and combustion models

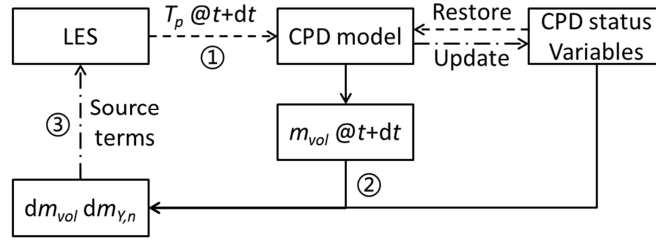
187 In this section, two pyrolysis models, i.e., the CPD and SFOM models, and the kinetic/diffusion
188 surface reaction model for char oxidation are introduced.

189 The CPD model, proposed by Fletcher et al. [26,43,44], is directly incorporated into the LES
190 framework to model the pyrolysis process of each coal particle. As one of the current state-of-the-art
191 coal pyrolysis models, the CPD model is able to describe the formation of volatile (including light
192 gases and heavy tar) based on the unique chemical structure of different coals. Its performance on
193 predicting the pyrolysis rate and volatile yield composition has been validated over a wide range of
194 heating rates, temperatures and coal ranks [26,43-46]. In our first-stage work [41,47], the CPD model
195 was used to model the pyrolysis of a single coal particle under various operating conditions, and
196 good agreement with experimental data was achieved on key pyrolysis results such as the time
197 history of the particle residual mass and the temperature at the particle center. The method of
198 incorporating the CPD model into the LES solver has been detailed in [27]. It is briefly repeated here
199 for completeness.

200 The CPD model was originally developed to predict the volatile yields with time. It has been
201 incorporated into the LES framework in the following way. Variables that represent the particle
202 pyrolysis status in the original CPD model are recorded and updated at every time step for each
203 particle. As shown in Fig. 4, with the particle temperature T_p at time $t + dt$ obtained, the CPD status
204 variables at the previous time t of this particle will be restored into the CPD model. Then the CPD
205 model can predict the total volatile yields of the particle at $t + dt$ according to the instantaneous
206 heating rate of the particle. Because we know the total volatile yields at the previous time t from the
207 recorded CPD status variables, the volatile release of the particle in the present time step dt can then

208 be calculated. Finally, the mass and species source terms due to pyrolysis can then be computed and
 209 the CPD status variables of the particle at time $t + dt$ will be updated for use at the next time step.
 210 The same procedure will be used for all the particles in the computational domain. It should be
 211 pointed out that the feasibility of directly incorporating the CPD model into a LES flow and
 212 combustion solver opens up a new route for further exploring physical mechanisms behind complex
 213 phenomena in pulverized-coal combustion. Release of harmful intermediate and minor species such
 214 as alkali metal or NO_x during pulverized-coal combustion is one such example.

215



216

217

Fig. 4. Coupling between the CPD model and the LES framework [27].

218

219 The single first-order reaction model or SFOM proposed by Badzioch & Hawskley [23] has
 220 been widely employed to model the pyrolysis of a pulverized-coal particle in PCC simulations:

221
$$\frac{dm_{vol}}{dt} = K_v (m_{vol}^* - m_{vol}) \quad , \quad (7)$$

222
$$K_v = A_v \exp\left(-\frac{E_v}{RT_p}\right) \quad , \quad (8)$$

223
$$m_{vol}^* = Qm_{vol}^{**} \quad , \quad (9)$$

224 where m_{vol} denotes the mass of the volatile yields at the current time step (kg), m_{vol}^* is the mass of
 225 the final volatile yields (kg), and m_{vol}^{**} is the mass of volatile matter in the proximate analysis (kg).

226 K_v is the pyrolysis rate coefficient (s^{-1}), R is the gas constant (8.314 J/mol K), A_v and E_v are the
 227 pre-exponential factor (s^{-1}) and activation energy (J/mol), respectively. The Q -factor in Eq. (9)

228 accounts for the increase of volatile yields due to a higher heating rate than in the proximate analysis
229 [22]. Differing from the CPD model, the kinetic parameters, i.e., A_v , E_v and Q , of the SFOM model
230 are not generic. Therefore this model is valid only for the conditions and coals on which it is
231 calibrated [24].

232 During pyrolysis, the coal particle diameter will swell, which is modeled as a linear function of
233 the extent of volatile release with the swelling coefficient set as 1.1. After the volatile matter is
234 completely released, heterogeneous combustion of the residual char occurs. The char oxidation
235 reaction is assumed to be $C (s) + 0.5 O_2 \rightarrow CO$. The kinetic/diffusion surface reaction model
236 proposed by Baum & Street [29] is employed. This model has considered both the intrinsic chemical
237 reaction on the internal surface of a char particle and the diffusion of gaseous oxidant through the
238 film layer around the particle. The experimental data suggest that char conversion is limited in this
239 pulverized-coal jet flame [4]. Therefore, for simplicity char gasification is not considered and char
240 combustion is assumed to start following the completion of pyrolysis in the present study, as in Stein
241 et al. [4].

242

243 *3.4. Gas phase combustion*

244 The volatile species are determined by the CPD pyrolysis model. As in [27], the light gases of
245 the volatile comprise H_2O , CO_2 , CH_4 , CO , C_2H_2 , and H_2 , and tar has a formula of $C_{16}H_{24}$. The
246 combustion of both the volatile species and the methane pilot is modeled using LES-PaSR [30] with
247 a two-step reaction mechanism for methane [48] and a one-step reaction mechanism [48,49] for the
248 other species (CO , C_2H_2 , H_2 and tar). These simplified reaction mechanisms have been widely
249 employed in both premixed [50] and non-premixed [51] combustion simulations and shown to be

250 able to correctly predict the main flame characteristics.

251 In the PaSR model, which has been used in LES of both premixed [52] and non-premixed [53]
252 combustion, each LES cell is viewed as a partially stirred reactor containing fine structures, where
253 most of the chemical reactions take place, and the surroundings. The volume fraction of the fine
254 structures can be estimated as $\kappa = \tau_c / (\tau_c + \tau_m)$ [30]. τ_c is a chemical time scale and modeled as $\tau_c = \delta_u$
255 / s_u , where $\delta_u \approx \nu / s_u$ is the laminar flame thickness, ν the kinematic viscosity, s_u the laminar flame
256 speed. τ_m is a subgrid mixing time scale and estimated as $\tau_m = \sqrt{\tau_K \tau_\Delta}$, where $\tau_K = (\nu / \varepsilon)^{1/2}$ is the
257 Kolmogorov time scale, $\tau_\Delta = \Delta / v'$ is the characteristic time scale of the subgrid velocity stretch, Δ
258 is the LES filter width, $v' = (2k/3)^{1/2}$ the subgrid velocity fluctuation. Finally, k and ε are the
259 subgrid turbulent kinetic energy (TKE) and its dissipation, which can be calculated as:
260 $k = 18\Delta^2 C_s^{4/3} \tilde{S}_{ij} \tilde{S}_{ij} / 4\pi^{2/3}$, $\varepsilon = 8\pi k^{3/2} / 27\Delta$, where \tilde{S}_{ij} is the strain rate tensor, C_s is the Smagorinsky
261 model coefficient which can be obtained from the Germano dynamic model [36]. After the reacting
262 volume fraction κ has been determined, the filtered reaction rate can then be modeled as
263 $\bar{\omega}_{Y,n} \approx \kappa \dot{\omega}(\bar{\rho}, \tilde{Y}_n, \tilde{T})$.

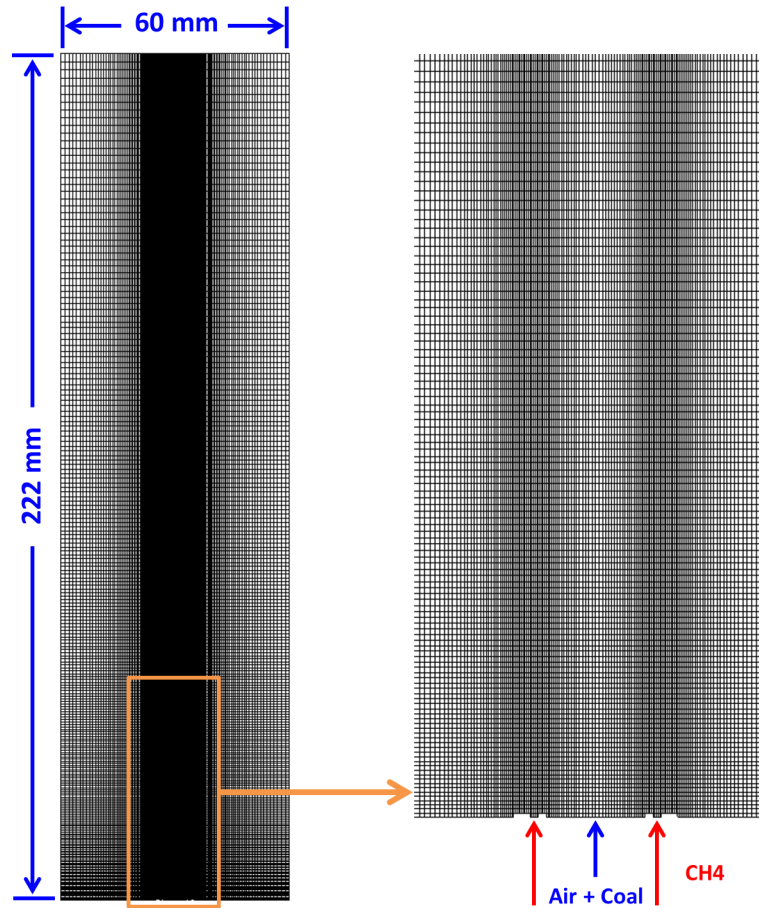
264

265 3.5. Computational setup

266 The computational domain size is 222 mm in length and 60 mm in width (Fig. 5). Both a
267 baseline- and a fine-grid case, which uses 1.6 million and 3.2 million cells, respectively, were
268 simulated to ensure that the LES results are only weakly sensitive to the computational grids used.
269 The minimum grid spacing for the two cases is 0.1 mm and 0.06 mm at the edge of the nozzle, and
270 the maximum is 2.2 mm and 1.3 mm at the downstream exit of the domain, respectively. For the
271 fine-grid case, only 0.03% of the grid cells which contain particles reach a relatively high particle

272 volume fraction between 5% and 22%, while ~97% of the grid cells have a particle volume fraction
273 lower than 1%. Therefore neglecting the solid volume fraction and using the Lagrangian point-source
274 approach for pulverized-coal particles is acceptable. A particle size distribution given by Bermúdez
275 et al. [31] is employed at the inlet. The particle size distribution is approximated by 6 different
276 diameters. When a new particle is injected, its diameter is randomly chosen to be one of the 6 with
277 the probability depending on the number percentage. The number mean (D10) and Sauter mean
278 diameters (SMD or D32) of the injected particles are 25 μm and 33 μm , respectively. The
279 characteristic Stokes number based on D10 of the injected particles is 3.3. In the simulations, each
280 Lagrangian particle represents a physical coal particle, and in total ~0.28 million particles are tracked
281 in the computational domain. An air co-flow with a small velocity (0.6 m/s) at room temperature is
282 setup surrounding the flame [4,17]. A separate, pre-processed pipe-flow LES with periodic
283 streamwise boundary conditions was used to provide turbulent inflow boundary conditions for the
284 gas phase [27].

285



286

287 Fig. 5. Computational domain and baseline-grid distribution. The central region near the nozzle is
 288 zoomed in and shown on the right side.

289

290 *3.6. Numerical schemes*

291 The time advancement uses a second-order Crank-Nicolson scheme. A third-order weighted
 292 essentially non-oscillatory (WENO) scheme [54] is used for the scalar advection terms in the species
 293 and temperature equations, while a second-order central difference scheme for the scalar diffusion
 294 terms in the species and temperature equations and all terms in the momentum equation. The gas
 295 phase equations are solved in cylindrical coordinates to take advantage of symmetries in the
 296 azimuthal direction, while pulverized-coal particles are traced in Cartesian coordinates. The particle
 297 equations are explicitly advanced using a second-order Runge-Kutta (RK2) scheme. Since the gas

298 phase and the particles are solved in different coordinate systems, the gas phase variables and
299 particle source terms have been mapped between the two coordinates at the same physical location of
300 a pulverized-coal particle. The Lagrangian point source terms of each particle are distributed onto the
301 8 surrounding grid points using a geometrical weighting. The Eulerian terms are interpolated to the
302 location of a Lagrangian point particle by performing a tri-linear interpolation with the 8 surrounding
303 grid points. An Alternating Direction Implicit (ADI) method has been employed where semi-implicit
304 tridiagonal/pentadiagonal equations are solved separately for each direction.

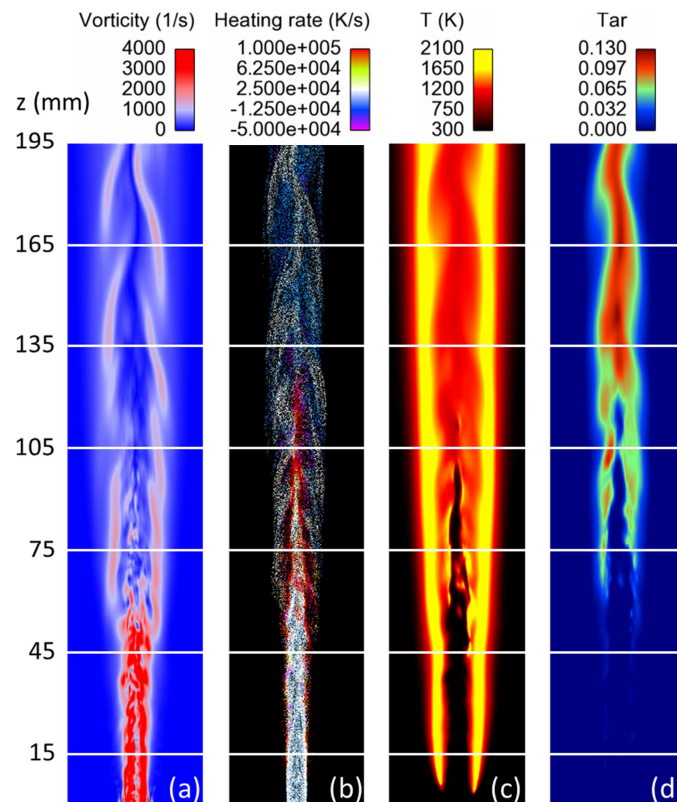
305

306 **4. Results and discussion**

307 *4.1. Characteristics of the two-phase jet flame*

308 Figure 6 shows the instantaneous fields of the vorticity, particle heating rate, gas temperature
309 and tar mass fraction of the pulverized-coal jet flame. The high temperature at the periphery of the jet
310 flow (Fig. 6c), especially in the upstream region ($z < 45$ mm), is mainly due to the methane pilot
311 flame. Coal particles injected from the central nozzle are gradually heated up (Fig. 6b) and tar (one
312 of the major volatile species) starts to be released from coal particles (Fig. 6d). In the region of $z =$
313 45-105 mm, more and more particles experience a high heating rate because of the heated central
314 region of the pulverized-coal jet flow. In addition, reaction of the gaseous volatile species released
315 during the heating process also occurs in the central region of the jet (Fig. 6c), which enhances the
316 heating and pyrolysis of coal particles in turn. Volatile combustion leads to the increase of the gas
317 temperature and the decrease of the gas-phase Reynolds number. Hence the vorticity of the gas flow
318 decreases (Fig. 6a). In the downstream region ($z > 105$ mm), the temperature in the central region
319 does not change significantly (Fig. 6c), although the mass fractions of volatile species are still high

320 (Fig. 6d). This is because most of the oxygen has been consumed (see Section 4.3) and therefore
 321 volatile combustion becomes weak. As shown in Fig. 6b, the particle-heating rate is considerably
 322 affected by the local flow conditions and carrier-phase temperature, and varies over a wide range of
 323 magnitudes. Considering the sensitivity of coal-particle pyrolysis kinetics to the local heating rate, it
 324 is easy to deduce that the pyrolysis characteristics of the coal particles will also vary and the CPD
 325 model should give more accurate predictions than a single-rate reaction mechanism, as will be shown
 326 later.
 327

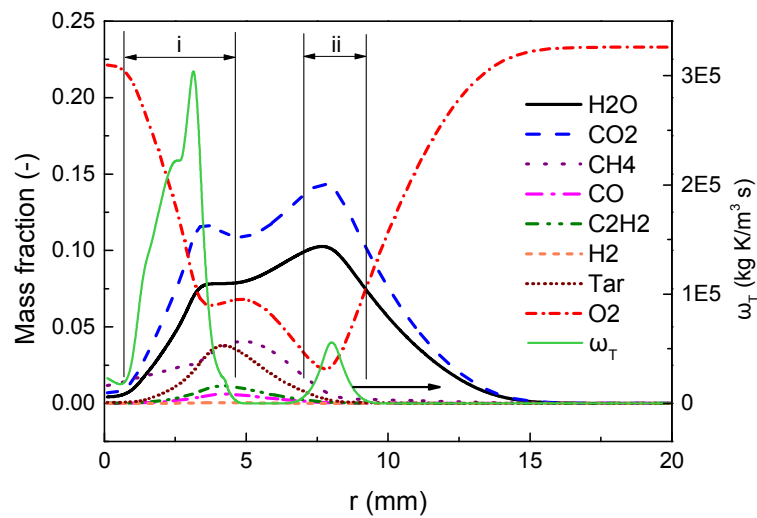


328
 329 Fig. 6. Instantaneous fields of the (a) vorticity, (b) particle heating rate, (c) gas temperature, and (d)
 330 tar mass fraction.

331
 332 In order to understand the combustion characteristics of the pulverized-coal jet flame, the radial
 333 profiles of the mean mass fractions of the products (H_2O and CO_2), fuel gases (CH_4 , CO , C_2H_2 , H_2

334 and tar), and the oxidizer (O_2), together with the mean chemical reaction source term in the
 335 temperature equation, i.e., ω_T , at $z = 60$ mm are shown in Fig. 7. It can be found that CH_4 and tar are
 336 the two major fuels. From the profile of the heat release rate ω_T , the gaseous fuels are found to
 337 mainly burn in two reaction regions, which are indicated by (i) and (ii) in Fig. 7. In region (i), Y_{O_2}
 338 decreases and the mass fractions of the gaseous fuels increase with r , indicating an overall diffusion
 339 flame structure predicted by the PaSR model. For region (ii), in its inner layer both Y_{O_2} and the mass
 340 fractions of the gaseous fuels decrease with r , indicating an overall premixed flame structure;
 341 whereas Y_{O_2} increases and the mass fractions of the gaseous fuels decrease with r in the outer layer,
 342 indicating an overall diffusion flame structure predicted by the PaSR model.

343



344

345 Fig. 7. Radial profiles of mean mass fractions of H_2O , CO_2 , CH_4 , CO , C_2H_2 , H_2 , tar and O_2 , and the
 346 mean chemical reaction source term ω_T in temperature equation at $z = 60$ mm. (i) and (ii) indicate the
 347 two reaction-active regions.

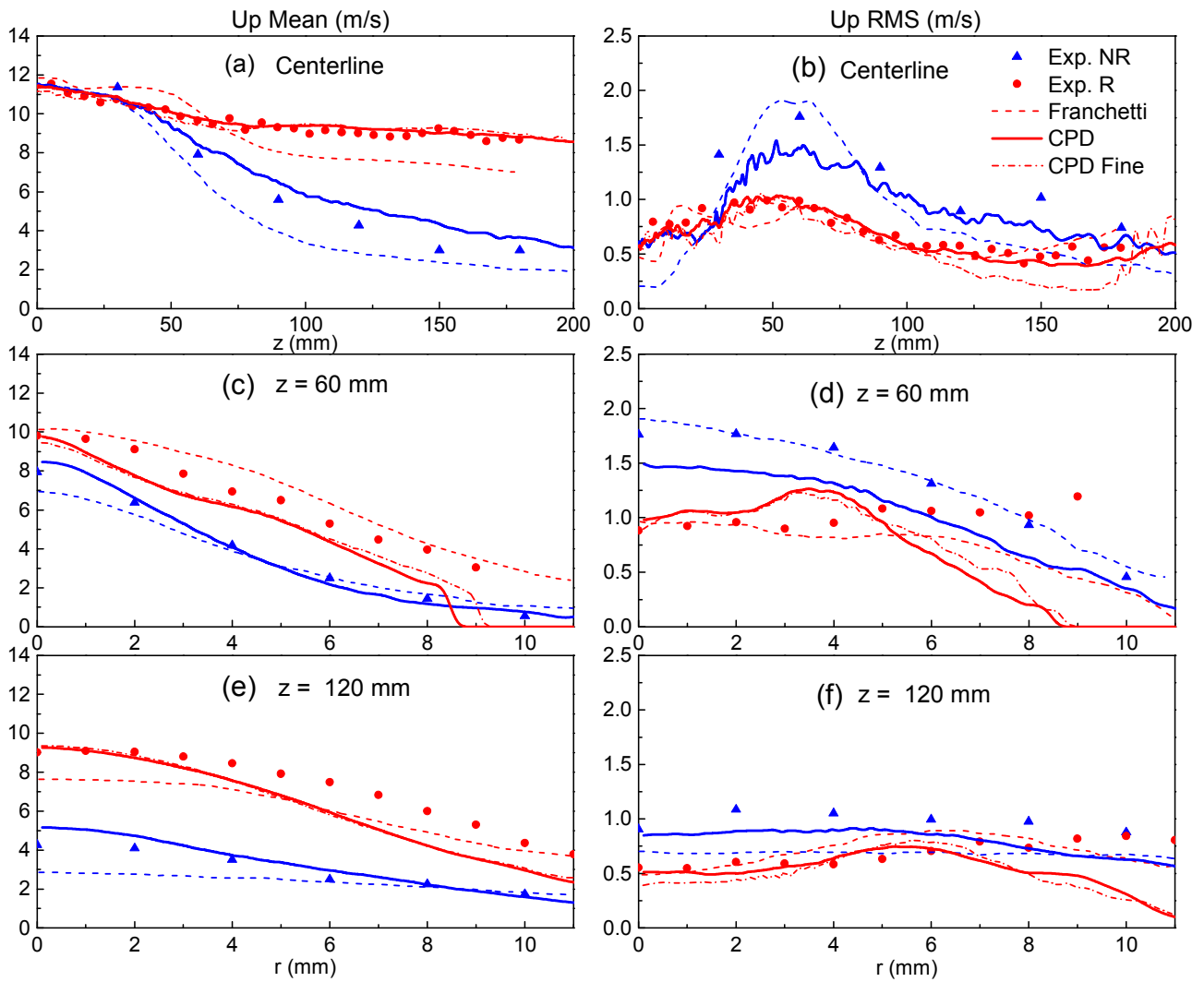
348

349 4.2. Particle statistics

350 Figure 8 compares the particle velocity statistics predicted by the CPD-incorporated LES

351 (CPD-LES) with the experimental data [16] and the LES results of Franchetti et al. (LES-B.M.F)
352 [17]. In the non-reacting case, the profiles of both LES simulations match the experimental data well,
353 although on the centerline the CPD-LES slightly over-predict the mean streamwise particle velocity,
354 while the LES-B.M.F under-predicts the velocity magnitude. One reason can be that the airflow rate
355 has been slightly adjusted in the present work to better approximate the actual experimental
356 condition. In the reacting case, the CPD-LES achieves a better agreement with the experimental data,
357 especially for the mean streamwise particle velocity on the centerline. For the radial profiles at the
358 two downstream locations, the results of the CPD-LES are slightly under-predicted for the mean
359 particle velocity; while for the RMS velocity, the agreement between the CPD-LES and experimental
360 data is good near the centerline, but becomes worse at the periphery of the jet. It can be found that
361 both the mean and RMS velocities decrease earlier at the jet periphery in the simulation than in the
362 measurement, especially at $z = 60$ mm, which indicates that the dispersion of coal particles in the
363 radial direction is under-estimated [19]. The difference of the simulation results between the
364 baseline- and fine-grid CPD-LES is small, demonstrating the LES results is only weakly sensitive to
365 the two grids. Overall, the comparison between the CPD-LES and experimental data is good, which
366 indicates the two-phase flow field has been properly predicted.

367



368

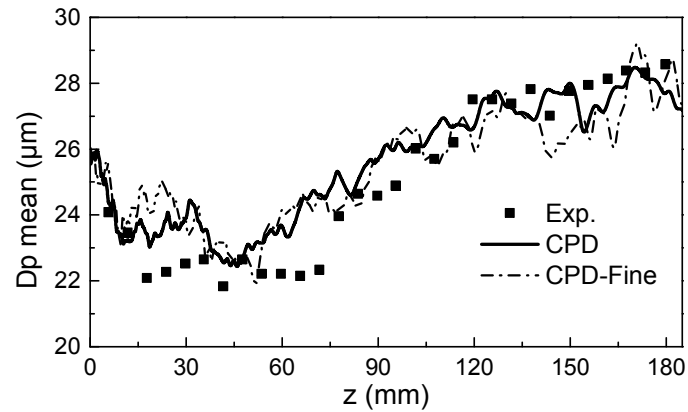
369 Fig. 8. Comparison of the mean (left) and RMS (right) streamwise velocities of the coal particles for
 370 both the reacting (R) and non-reacting (NR) cases on the centerline (a-b) and at two downstream
 371 locations (c-d: 60 mm from the nozzle inlet; e-f: 120 mm from the nozzle inlet).

372

373 Figure 9 compares the mean particle diameters (the number mean, i.e., D10) along the centerline
 374 between the CPD-LES prediction and experimental data under reacting conditions. After a slight
 375 drop, the mean particle diameter continues to increase along the jet centerline. This can be attributed
 376 to two reasons. First, smaller particles tend to disperse away from the centerline. Second, coal
 377 particles swell as the pyrolysis progresses. The results of the CPD-LES show this trend well and
 378 achieve a close match with the experimental data. The agreement also suggests that pyrolysis of coal

379 particles is well predicted, because the prediction of particle swelling is fully based on the extent of
380 pyrolysis.

381



382

383 Fig. 9. Comparison of the mean diameter of coal particles along the centerline for the reacting case.

384

385 4.3. Mole fractions of species

386 Figure 10 compares the mole fractions of O_2 and CO_2 along the centerline predicted by the
387 CPD-LES and LES-B.M.F [17] with the experimental data. It can be found that the CPD-LES
388 achieves a better agreement with experimental data than the LES-B.M.F. To understand the cause of
389 the improvement, two other simulation cases (SFOM-LES and EBU-LES) have also been set up. The
390 SFOM-LES case uses the same setup as the CPD-LES case except that the SFOM model is
391 employed for pyrolysis modeling; while the EBU-LES case employs the SFOM model for pyrolysis
392 and the EBU model for gas phase combustion. The kinetic parameters of the SFOM model are
393 calibrated by an offline CPD model and preset, and identical for each particle [4,17]. The detailed
394 procedure of the calibration can be found in our previous study [27] and the obtained kinetic
395 parameters are A_v ($4.5 \times 10^3 \text{ s}^{-1}$), E_v ($1.92 \times 10^4 \text{ J/mol}$) and Q (1.52).

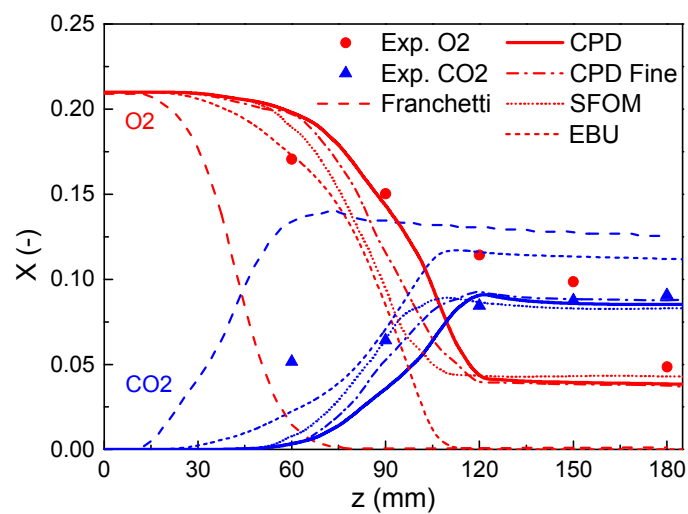
396 Comparing the results between the CPD-LES and CPD-calibrated SFOM-LES, the prediction of

397 the O₂ consumption in the CPD-LES case is closer to the experimental data, while that of CO₂
 398 production tends to be under-predicted. In other words, the SFOM-LES predicts a faster combustion
 399 process of volatile species.

400 The influence of the subgrid gas-phase combustion models on the simulation can be revealed by
 401 comparing the results between SFOM-LES and EBU-LES, in which the PaSR and EBU models are
 402 used, respectively. Due to the assumption of infinitely fast chemistry, the EBU model tends to
 403 over-estimate O₂ consumption and CO₂ production. Franchetti et al. [17] therefore recommended
 404 finite-rate chemistry models for volatile combustion. The PaSR model takes into consideration
 405 subgrid turbulence-chemistry interactions by estimating the reacting volume fraction κ of the
 406 filtering volume based on a subgrid mixing time scale and a chemical time scale, and therefore yields
 407 a better agreement with the experimental data.

408 Finally, it should be pointed out that the LES results of the mole fractions of N₂ + H₂O also
 409 agree well with the experimental data (not shown here).

410



411

412

Fig. 10. Comparison of the mole fractions of O₂ and CO₂ along the centerline.

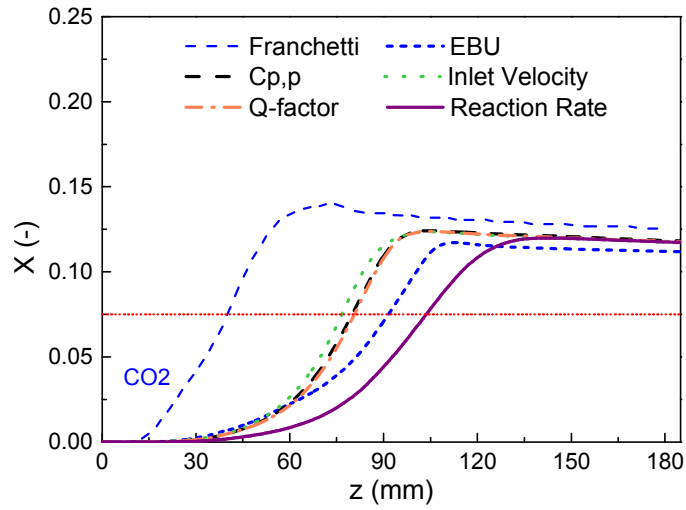
413

414 4.4. Sensitivity analysis

415 It has been found in Fig. 10 that the results of the EBU-LES in the present work are closer to
416 those of the CPD-LES than those of the LES-B.M.F, although the same pyrolysis and gas phase
417 combustion models have been employed in both the EBU-LES and the LES-B.M.F. In order to
418 understand the reason of the difference between EBU-LES and LES-B.M.F, parametric studies with
419 different settings have been performed to investigate the impact of the heat capacity of coal particles,
420 the adjustment of the air flow rate (the inlet velocity), the Q -factor value in the SFOM model and the
421 reaction rate coefficient in the EBU combustion model on the prediction of the species.

422 Figure 11 compares the results of the four additional LES cases. Specifically, in the ‘Inlet
423 Velocity’ case, the air flow rate of the primary inlet has been set to the original value, i.e., 1.80×10^{-4}
424 m^3/s (13% lower), which is the value used in LES-B.M.F; in the ‘ Q -factor’ case, the Q -factor value
425 in the SFOM model has been set to 1.9 (25% higher), which is the value used in LES-B.M.F; in the
426 ‘ $C_{p,p}$ ’ case, the heat capacity of a pulverized-coal particle has been decreased by 30% (the value used
427 in LES-B.M.F was not reported); in the ‘Reaction Rate’ case, the homogeneous reaction rate
428 predicted by the EBU model has been decreased by 50%. It can be seen that the adjustment of the
429 heat capacity of coal particles, the air flow rate (inlet velocity), the Q -factor in the SFOM model and
430 the reaction rate coefficient in the EBU model all considerably affect the profiles of the mole fraction
431 of CO_2 , X_{CO_2} .

432



433

434 Fig. 11. The impact of heat capacity of coal particle (30% lower), inlet velocity (13% lower), the
 435 Q -factor value in SFOM model (25% higher) and reaction rate (50% lower) on the prediction of the
 436 mole fractions of CO_2 along the centerline.

437

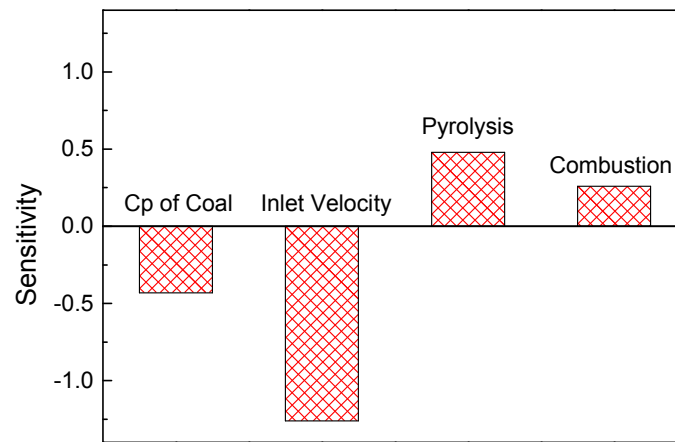
438 To quantify the influence of the four investigated parameters on the LES predictions, sensitivity
 439 analysis has been performed (Fig. 12). Sensitivity is estimated based on the distance from the nozzle
 440 to the downstream location where the mole fraction of CO_2 reaches 0.075 on the centerline (the red
 441 dotted line in Fig. 11):

$$442 \quad \text{Sensitivity} = \frac{z_{\text{CO}_2=0.075}(\text{original}) - z_{\text{CO}_2=0.075}(\text{additional})}{z_{\text{CO}_2=0.075}(\text{original}) \alpha(\text{additional})} \quad (10)$$

443 where ‘original’ refers to EBU-LES and ‘additional’ refers to the four additional LES cases.
 444 $\alpha(\text{additional})$ means the increased percentage of the investigated parameter of an additional case to
 445 the original EBU-LES. Specifically, $\alpha(\text{additional}) = -30\%$, -13% , 25% and -50% for the ‘ $C_{p,p}$ ’,
 446 ‘Inlet Velocity’, ‘ Q -factor’ and ‘Reaction Rate’ cases, respectively. The obtained sensitivity analysis
 447 results are shown in Fig. 12, which illustrates the effects of uncertainties in the heat capacity of coal
 448 particles, the inlet velocity, the pyrolysis model and the combustion model on the LES predictions.
 449 The sensitivity analysis indicates that the inlet velocity affects the LES results to the greatest degree,

450 which indicates the importance of inflow boundary conditions for the case studied.

451



452

453 Fig. 12. Sensitivity analysis that compares the uncertainties of heat capacity of coal particles, inlet
454 velocity, and pyrolysis and combustion models on the LES predictions.

455

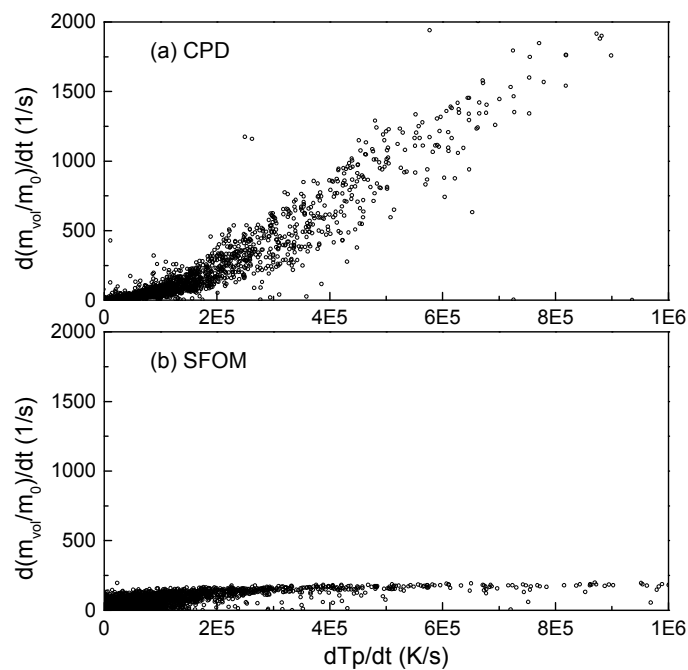
456 4.5. Instantaneous particle pyrolysis characteristics

457 Although the CPD-LES and SFOM-LES showed similar predictions on the mean mole fractions
458 of O_2 and CO_2 , the scatter plots in Fig. 13 show very different instantaneous correlations between the
459 local heat rate and the normalized pyrolysis rate of a coal particle. For all the particles shown in Fig.
460 13, the particle temperatures are $T_p \in [1075, 1125]$ K, in which coal particle pyrolysis actively
461 occurs. In the CPD-LES (Fig. 13a), the local heating rate of a coal particle is found to have a strong
462 correlation with its pyrolysis rate. A higher heating rate leads to a higher pyrolysis rate. On the other
463 hand, in the SFOM-LES (Fig. 13b), the pyrolysis rate of a coal particle is shown to be largely
464 independent of the heating rate. It is clear that the incorporated CPD model can adjust the pyrolysis
465 kinetics of coal particles according to the local heating rate, while the SFOM model does not have
466 this online adjusting capacity. It should be noted that the SFOM-LES in the present study already
467 employed the Q -factor as one of the pyrolysis parameters, accounting for the increase of volatile

468 yields caused by a higher heating rate than in the proximate analysis [22], and the Q -factor had been
 469 also calibrated by the CPD model. However, the calibrated Q -factor (based on the averaged heating
 470 rate of coal particles) is identical for each particle and remains constant during the LES simulation.
 471 Because the SFOM pyrolysis model predicts the pyrolysis characteristics of coal particles based on
 472 empirical equations, it cannot fully model the underlying physical mechanisms of pyrolysis that has
 473 been considered in the CPD model.

474 To evaluate the computational cost of the CPD-LES method, the average wall-clock-time per
 475 time step of SFOM-LES and CPD-LES is recorded. The value is 6.27 s for SFOM-LES and 6.51 s
 476 for CPD-LES. And the time consumed by solving particle equations per time step is 0.26 s for
 477 SFOM-LES and 0.38 s for CPD-LES. Since the cost of solving particle equations is only a small
 478 proportion ($\sim 5\%$) of the overall cost, there is no significant increase of the computational cost for the
 479 CPD-LES method in the present study.

480



481

482 Fig. 13. Comparison of instantaneous particle pyrolysis characteristics between the (a) CPD-LES and

483 (b) SFOM-LES.

484

485 **5. Conclusions**

486 A CPD-incorporated LES (CPD-LES) method has been used to investigate a laboratory-scale
487 pulverized-coal jet flame. In this method, the CPD model (a detailed coal pyrolysis model) has been
488 incorporated into the LES framework directly. The instantaneous pyrolysis kinetics of each coal
489 particle can be provided by the CPD model during the simulation. Therefore the effects of the local
490 heating rate on the pyrolysis of a coal particle can be considered. Volatile combustion is modeled
491 using the PaSR model, in which the reaction rate is determined based on both a turbulent mixing
492 time scale and a chemical time scale. The kinetic/diffusion surface reaction model has been used for
493 char combustion, incorporating both the intrinsic chemical reaction on the internal surface of a char
494 particle and the diffusion of gaseous oxidant through the film layer around the particle. The
495 CRIEPI's pulverized-coal jet flame is used for validating the CPD-LES method. Good agreements
496 between the experimental measurements and the CPD-LES results have been achieved on mean and
497 RMS particle velocities, mean particle diameters and species concentrations. Although the CPD-LES
498 shows a clear advantage in predicting instantaneous pyrolysis of coal particles, predictions of the
499 mean mole fractions of major species are only marginally improved. To better understand the effects
500 of parameter uncertainties on the LES results, sensitivity analysis has been performed on the heat
501 capacity of coal particles, the inlet velocity, the kinetic parameter in the pyrolysis (SFOM) model and
502 the reaction rate of the combustion (EBU) model. It was found that all these parameters considerably
503 affect the predictions on the major species, and the inlet velocity boundary condition shows a
504 dominant role in the quantified uncertainty analysis.

505

506 **Acknowledgements**

507 This work was performed by the first author KDW when he was a Research Assistant at Brunel
508 University London under the support of the Engineering and Physical Sciences Research Council
509 (EPSRC) of the UK and the China Scholarship Council. The research was also supported by the
510 National Natural Science Foundation of China (51422605, 51390491) and National Basic Research
511 Program of China (2012CB214906). This work used the ARCHER UK National Supercomputing
512 Service (<http://www.archer.ac.uk>).

513

514 **Compliance with Ethical Standards**

515 **Conflict of Interest:** The authors declare that they have no conflict of interest.

516

517 **References**

- 518 1. Khatami, R., Levendis, Y.A.: An overview of coal rank influence on ignition and combustion
519 phenomena at the particle level. *Combust. Flame* **164**, 22-34 (2016).
520 doi:<http://dx.doi.org/10.1016/j.combustflame.2015.10.031>
- 521 2. Vascellari, M., Schulze, S., Nikrityuk, P., Safronov, D., Hasse, C.: Numerical Simulation of
522 Pulverized Coal MILD Combustion Using a New Heterogeneous Combustion Submodel. *Flow*
523 *Turbul. Combust.* **92**(1), 319-345 (2014). doi:10.1007/s10494-013-9467-7
- 524 3. Knappstein, R., Kuenne, G., Ketelheun, A., Köser, J., Becker, L., Heuer, S., Schiemann, M.,
525 Scherer, V., Dreizler, A., Sadiki, A., Janicka, J.: Devolatilization and volatiles reaction of
526 individual coal particles in the context of FGM tabulated chemistry. *Combust. Flame* **169**, 72-84
527 (2016). doi:<http://dx.doi.org/10.1016/j.combustflame.2016.04.014>
- 528 4. Stein, O.T., Olenik, G., Kronenburg, A., Marincola, F.C., Franchetti, B.M., Kempf, A.M., Ghiani,
529 M., Vascellari, M., Hasse, C.: Towards comprehensive coal combustion modelling for LES. *Flow*
530 *Turbul. Combust.* **90**(4), 859-884 (2013).
- 531 5. Li, M., Zhang, L.: Haze in China: Current and future challenges. *Environ. Pollut.* **189**, 85-86
532 (2014). doi:<http://dx.doi.org/10.1016/j.envpol.2014.02.024>
- 533 6. Hees, J., Zabrodiec, D., Massmeyer, A., Habermehl, M., Kneer, R.: Experimental Investigation
534 and Comparison of Pulverized Coal Combustion in CO₂/O₂- and N₂/O₂-Atmospheres. *Flow*
535 *Turbul. Combust.* **96**(2), 417-431 (2016). doi:10.1007/s10494-015-9662-9
- 536 7. Mei, Z., Li, P., Mi, J., Wang, F., Zhang, J.: Diffusion MILD Combustion of Firing Pulverized-coal

- 537 at a Pilot Furnace. *Flow Turbul. Combust.* **95**(4), 803-829 (2015).
538 doi:[10.1007/s10494-015-9642-0](https://doi.org/10.1007/s10494-015-9642-0)
- 539 8. Kurose, R., Makino, H.: Large eddy simulation of a solid-fuel jet flame. *Combust. Flame* **135**(1–2),
540 1-16 (2003). doi:[http://dx.doi.org/10.1016/S0010-2180\(03\)00141-X](http://dx.doi.org/10.1016/S0010-2180(03)00141-X)
- 541 9. Kurose, R., Watanabe, H., Makino, H.: Numerical simulations of pulverized coal combustion.
542 *KONA Powder Part. J.* **27**, 144-156 (2009).
- 543 10. Edge, P., Gubba, S.R., Ma, L., Porter, R., Pourkashanian, M., Williams, A.: LES modelling of air
544 and oxy-fuel pulverised coal combustion—impact on flame properties. *Proc. Combust. Inst.*
545 **33**(2), 2709-2716 (2011).
- 546 11. Gharebaghi, M., Irons, R.M.A., Ma, L., Pourkashanian, M., Pranzitelli, A.: Large eddy
547 simulation of oxy-coal combustion in an industrial combustion test facility. *Int. J. Greenh. Gas*
548 *Control* **5**, S100-S110 (2011).
- 549 12. Chen, L., Ghoniem, A.F.: Simulation of oxy-coal combustion in a 100 kWth test facility using
550 RANS and LES: a validation study. *Energy Fuels* **26**(8), 4783-4798 (2012).
- 551 13. Yamamoto, K., Murota, T., Okazaki, T., Taniguchi, M.: Large eddy simulation of a pulverized
552 coal jet flame ignited by a preheated gas flow. *Proc. Combust. Inst.* **33**(2), 1771-1778 (2011).
- 553 14. Pedel, J., Thornock, J.N., Smith, P.J.: Large eddy simulation of pulverized coal jet flame ignition
554 using the direct quadrature method of moments. *Energy Fuels* **26**(11), 6686-6694 (2012).
- 555 15. Taniguchi, M., Okazaki, H., Kobayashi, H., Azuhata, S., Miyadera, H., Muto, H., Tsumura, T.:
556 Pyrolysis and ignition characteristics of pulverized coal particles. *J. Energy Resour. Technol.*
557 **123**(1), 32-38 (2001).
- 558 16. Hwang, S.M., Kurose, R., Akamatsu, F., Tsuji, H., Makino, H., Katsuki, M.: Application of
559 optical diagnostics techniques to a laboratory-scale turbulent pulverized coal flame. *Energy Fuels*
560 **19**(2), 382-392 (2005).
- 561 17. Franchetti, B.M., Cavallo Marincola, F., Navarro-Martinez, S., Kempf, A.M.: Large eddy
562 simulation of a pulverised coal jet flame. *Proc. Combust. Inst.* **34**(2), 2419-2426 (2013).
- 563 18. Rabaçal, M., Franchetti, B.M., Marincola, F.C., Proch, F., Costa, M., Hasse, C., Kempf, A.M.:
564 Large Eddy Simulation of coal combustion in a large-scale laboratory furnace. *Proc. Combust.*
565 *Inst.* **35**(3), 3609-3617 (2015). doi:<http://dx.doi.org/10.1016/j.proci.2014.06.023>
- 566 19. Hara, T., Muto, M., Kitano, T., Kurose, R., Komori, S.: Direct numerical simulation of a
567 pulverized coal jet flame employing a global volatile matter reaction scheme based on detailed
568 reaction mechanism. *Combust. Flame* **162**(12), 4391-4407 (2015).
569 doi:<http://dx.doi.org/10.1016/j.combustflame.2015.07.027>
- 570 20. Watanabe, J., Yamamoto, K.: Flamelet model for pulverized coal combustion. *Proc. Combust.*
571 *Inst.* **35**(2), 2315-2322 (2015). doi:<http://dx.doi.org/10.1016/j.proci.2014.07.065>
- 572 21. Zhao, X.Y., Haworth, D.C.: Transported PDF modeling of pulverized coal jet flames. *Combust.*
573 *Flame* **161**(7), 1866-1882 (2014).
- 574 22. Hashimoto, N., Kurose, R., Shirai, H.: Numerical simulation of pulverized coal jet flame
575 employing the TDP model. *Fuel* **97**, 277-287 (2012).
576 doi:<http://dx.doi.org/10.1016/j.fuel.2012.03.005>
- 577 23. Badzioch, S., Hawksley, P.G.W.: Kinetics of thermal decomposition of pulverized coal particles.
578 *Ind. Eng. Chem. Proc. Des. Dev.* **9**(4), 521-530 (1970).
- 579 24. Vascellari, M., Arora, R., Pollack, M., Hasse, C.: Simulation of entrained flow gasification with
580 advanced coal conversion submodels. Part 1: Pyrolysis. *Fuel* **113**, 654-669 (2013).
- 581 25. Vascellari, M., Xu, H., Hasse, C.: Flamelet modeling of coal particle ignition. *Proc. Combust.*

- 582 Inst. **34**(2), 2445-2452 (2013).
- 583 26. Grant, D.M., Pugmire, R.J., Fletcher, T.H., Kerstein, A.R.: Chemical-Model of Coal
584 Devolatilization Using Percolation Lattice Statistics. *Energy Fuels* **3**(2), 175-186 (1989). doi:Doi
585 10.1021/Ef00014a011
- 586 27. Wan, K.D., Xia, J., Wang, Z.H., Wrobel, L.C., Cen, K.F.: Online-CPD-coupled large-eddy
587 simulation of pulverized-coal pyrolysis in a hot turbulent nitrogen jet. *Combust. Sci. Technol.*
588 (2016). doi:<http://dx.doi.org/10.1080/00102202.2016.1193498>
- 589 28. Magnussen, B.F., Hjertager, B.H.: On mathematical modeling of turbulent combustion with
590 special emphasis on soot formation and combustion. *Symp. (Int.) Combust.* **16**(1), 719-729
591 (1977). doi:[http://dx.doi.org/10.1016/S0082-0784\(77\)80366-4](http://dx.doi.org/10.1016/S0082-0784(77)80366-4)
- 592 29. Baum, M.M., Street, P.J.: Predicting the combustion behaviour of coal particles. *Combust. Sci.*
593 *Technol.* **3**(5), 231-243 (1971).
- 594 30. Berglund, M., Fedina, E., Fureby, C., Tegnér, J., Sabel'nikov, V.: Finite Rate Chemistry
595 Large-Eddy Simulation of Self-Ignition in Supersonic Combustion Ramjet. *AIAA J.* **48**(3),
596 540-550 (2010). doi:10.2514/1.43746
- 597 31. Bermúdez, A., Ferrín, J.L., Liñán, A., Saavedra, L.: Numerical simulation of group combustion
598 of pulverized coal. *Combust. Flame* **158**(9), 1852-1865 (2011).
599 doi:<http://dx.doi.org/10.1016/j.combustflame.2011.02.002>
- 600 32. Xia, J., Luo, K.H., Kumar, S.: Large-Eddy Simulation of Interactions Between a Reacting Jet and
601 Evaporating Droplets. *Flow Turbul. Combust.* **80**(1), 133-153 (2008).
602 doi:10.1007/s10494-007-9084-4
- 603 33. Xia, J., Luo, K.H., Zhao, H.: Dynamic Large-Eddy Simulation of Droplet Effects on a Reacting
604 Plume in Countercurrent Configuration. *Combust. Sci. Technol.* **183**(5), 487-518 (2011).
605 doi:10.1080/00102202.2010.534517
- 606 34. Xia, J., Zhao, H., Megaritis, A., Luo, K.H., Cairns, A., Ganippa, L.C.: Inert-droplet and
607 combustion effects on turbulence in a diluted diffusion flame. *Combust. Flame* **160**(2), 366-383
608 (2013). doi:<http://dx.doi.org/10.1016/j.combustflame.2012.10.007>
- 609 35. Yi, F.X.: Direct Numerical Simulation of Gas/Coal Particles Gas-Solid Two-Phase Round Jet
610 Combustion Flow. Ph.D. Thesis, Zhejiang University (2012 (in Chinese))
- 611 36. Germano, M., Piomelli, U., Moin, P., Cabot, W.H.: A dynamic subgrid - scale eddy viscosity
612 model. *Phys. Fluids A* **3**(7), 1760-1765 (1991).
- 613 37. Sutherland, W.: LII. The viscosity of gases and molecular force. *Philos. Mag.* **36**(223), 507-531
614 (1893). doi:10.1080/14786449308620508
- 615 38. Jones, W.P., Lyra, S., Navarro-Martinez, S.: Large Eddy Simulation of a swirl stabilized spray
616 flame. *Proc. Combust. Inst.* **33**(2), 2153-2160 (2011).
617 doi:<http://dx.doi.org/10.1016/j.proci.2010.07.032>
- 618 39. Ranz, W.E., Marshall, W.R.: Evaporation from drops. *Chem. Eng. Prog.* **48**(3), 141-146 (1952).
- 619 40. Chandrasekhar, S.: Radiative transfer. Dover Publications, New York (1960)
- 620 41. Wan, K.D., Wang, Z.H., He, Y., Xia, J., Zhou, Z.J., Zhou, J.H., Cen, K.F.: Experimental and
621 modeling study of pyrolysis of coal, biomass and blended coal-biomass particles. *Fuel* **139**,
622 356-364 (2015).
- 623 42. Smith, T.F., Shen, Z.F., Friedman, J.N.: Evaluation of Coefficients for the Weighted Sum of Gray
624 Gases Model. *J. Heat Transfer* **104**(4), 602-608 (1982). doi:10.1115/1.3245174
- 625 43. Fletcher, T.H., Kerstein, A.R., Pugmire, R.J., Grant, D.M.: Chemical percolation model for
626 devolatilization. 2. Temperature and heating rate effects on product yields. *Energy Fuels* **4**(1),

- 627 54-60 (1990).
- 628 44. Fletcher, T.H., Kerstein, A.R., Pugmire, R.J., Solum, M.S., Grant, D.M.: Chemical Percolation
629 Model for Devolatilization .3. Direct Use of C-13 Nmr Data to Predict Effects of Coal Type.
630 Energy Fuels **6**(4), 414-431 (1992). doi:Doi 10.1021/Ef00034a011
- 631 45. Genetti, D., Fletcher, T.H., Pugmire, R.J.: Development and application of a correlation of ¹³C
632 NMR chemical structural analyses of coal based on elemental composition and volatile matter
633 content. Energy Fuels **13**(1), 60-68 (1999).
- 634 46. Genetti, D.B.: An advanced model of coal devolatilization based on chemical structure. M.S.
635 Thesis, Brigham Young University (1999)
- 636 47. Wang, Z.H., Wan, K.D., Xia, J., He, Y., Liu, Y.Z., Liu, J.Z.: Pyrolysis Characteristics of Coal,
637 Biomass, and Coal–Biomass Blends under High Heating Rate Conditions: Effects of Particle
638 Diameter, Fuel Type, and Mixing Conditions. Energy Fuels **29**(8), 5036-5046 (2015).
639 doi:10.1021/acs.energyfuels.5b00646
- 640 48. Westbrook, C.K., Dryer, F.L.: Simplified Reaction Mechanisms for the Oxidation of
641 Hydrocarbon Fuels in Flames. Combust. Sci. Technol. **27**(1-2), 31-43 (1981).
642 doi:10.1080/00102208108946970
- 643 49. Milewski, J., Świrski, K., Santarelli, M., Leone, P.: Advanced methods of solid oxide fuel cell
644 modeling. Springer-Verlag London, (2011)
- 645 50. Duwig, C., Nogenmyr, K.-J., Chan, C.-k., Dunn, M.J.: Large Eddy Simulations of a piloted lean
646 premix jet flame using finite-rate chemistry. Combust. Theory Model. **15**(4), 537-568 (2011).
647 doi:10.1080/13647830.2010.548531
- 648 51. El-Asrag, H., Menon, S.: Large eddy simulation of bluff-body stabilized swirling non-premixed
649 flames. Proc. Combust. Inst. **31**(2), 1747-1754 (2007).
650 doi:<http://dx.doi.org/10.1016/j.proci.2006.07.251>
- 651 52. Sabelnikov, V., Fureby, C.: LES combustion modeling for high Re flames using a multi-phase
652 analogy. Combust. Flame **160**(1), 83-96 (2013).
653 doi:<http://dx.doi.org/10.1016/j.combustflame.2012.09.008>
- 654 53. Moule, Y., Sabelnikov, V., Mura, A.: Highly resolved numerical simulation of combustion in
655 supersonic hydrogen–air coflowing jets. Combust. Flame **161**(10), 2647-2668 (2014).
656 doi:<http://dx.doi.org/10.1016/j.combustflame.2014.04.011>
- 657 54. Liu, X.D., Osher, S., Chan, T.: Weighted essentially non-oscillatory schemes. J. Comput. Phys.
658 **115**(1), 200-212 (1994).
- 659

Figure captions

Fig. 1. The inlet nozzle of the CRIEPI burner. Methane flow rate: $2.33 \times 10^{-5} \text{ m}^3/\text{s}$; pulverized-coal feeding rate: $1.49 \times 10^{-4} \text{ kg/s}$; air flow rate: $2.07 \times 10^{-4} \text{ m}^3/\text{s}$. The air flow rate has been adjusted by taking into consideration the air aspirated from the pulverized-coal feeder [22], and the Reynolds number is ~ 2900 .

Fig. 2. Comparison of LES results on the mean and RMS streamwise velocities of coal particles and the mole fractions of O_2 and CO_2 along the jet centerline between two cases with unity and variable Lewis numbers.

Fig. 3. Comparison of LES results on the mean and RMS streamwise velocities of coal particles along the jet centerline and at $z = 60 \text{ mm}$ between two cases with the stochastic Markov model enabled and disabled.

Fig. 4. Coupling between the CPD model and the LES framework [27].

Fig. 5. Computational domain and baseline-grid distribution. The central region near the nozzle is zoomed in and shown on the right side.

Fig. 6. Instantaneous fields of the (a) vorticity, (b) particle heating rate, (c) gas temperature, and (d) tar mass fraction.

Fig. 7. Radial profiles of mean mass fractions of H_2O , CO_2 , CH_4 , CO , C_2H_2 , H_2 , tar and O_2 , and the mean chemical reaction source term ω_T in temperature equation at $z = 60 \text{ mm}$. (i) and (ii) indicate the two reaction-active regions.

Fig. 8. Comparison of the mean (left) and RMS (right) streamwise velocities of the coal particles for both the reacting (R) and non-reacting (NR) cases on the centerline (a-b) and at two downstream locations (c-d: 60 mm from the nozzle inlet; e-f: 120 mm from the nozzle inlet).

Fig. 9. Comparison of the mean diameter of coal particles along the centerline for the reacting case.

Fig. 10. Comparison of the mole fractions of O_2 and CO_2 along the centerline.

Fig. 11. The impact of heat capacity of coal particle (30% lower), inlet velocity (13% lower), the Q -factor value in SFOM model (25% higher) and reaction rate (50% lower) on the prediction of the mole fractions of CO_2 along the centerline.

Fig. 12. Sensitivity analysis that compares the uncertainties of heat capacity of coal particles, inlet velocity, and pyrolysis and combustion models on the LES predictions.

Fig. 13. Comparison of instantaneous particle pyrolysis characteristics between the (a) CPD-LES and (b) SFOM-LES.

Color figures can be used for the online PDF version and the gray style for hardcopy reproduction.